Mapping landslide displacements using Structure from Motion (SfM) and image correlation of multi-temporal UAV photography

Arko Lucieer, Steven M. de Jong and Darren Turner

Progress in Physical Geography 2014 38: 97 originally published online 24 December 2013
DOI: 10.1177/0309133313515293

Article

Progress in Physical Geography
2014, Vol. 38(1) 97–116

DOI: 10.1177/0309133313515293
ppg.sagepub.com
SAGE

Mapping landslide displacements using Structure from Motion (SfM) and image correlation of multi-temporal UAV photography

Arko Lucieer
University of Tasmania, Australia

Steven M. de Jong
Utrecht University, The Netherlands

Darren Turner
University of Tasmania, Australia

Abstract
In this study, we present a flexible, cost-effective, and accurate method to monitor landslides using a small unmanned aerial vehicle (UAV) to collect aerial photography. In the first part, we apply a Structure from Motion (SfM) workflow to derive a 3D model of a landslide in southeast Tasmania from multi-view UAV photography. The geometric accuracy of the 3D model and resulting DEMs and orthophoto mosaics was tested with ground control points coordinated with geodetic GPS receivers. A horizontal accuracy of 7 cm and vertical accuracy of 6 cm was achieved. In the second part, two DEMs and orthophoto mosaics acquired on 16 July 2011 and 10 November 2011 were compared to study landslide dynamics. The COSI-Corr image correlation technique was evaluated to quantify and map terrain displacements. The magnitude and direction of the displacement vectors derived from correlating two hillshaded DEM layers corresponded to a visual interpretation of landslide change. Results show that the algorithm can accurately map displacements of the toes, chunks of soil, and vegetation patches on top of the landslide, but is not capable of mapping the retreat of the main scarp. The conclusion is that UAV-based imagery in combination with 3D scene reconstruction and image correlation algorithms provide flexible and effective tools to map and monitor landslide dynamics.

Keywords
COSI-Corr, digital elevation model (DEM), Home Hill landslide, OktoKopter, orthophoto mosaic, Tasmania

I Introduction

Landslides are recognized as an important type of natural disaster worldwide and are a major hazard in most mountainous and hilly regions as well as in steep river banks and coastal slopes (Dikau et al., 1996; Guzzetti, 2000; Schuster and Fleming, 1986; Zillman, 1999). Significant

Corresponding author:
Arko Lucieer, University of Tasmania, School of Geography and Environmental Studies, Private Bag 76, Hobart, Tasmania 7001, Australia.
Email: arko.lucieer@utas.edu.au

human casualties and economic losses, largely as damage to infrastructure (roads, railways, pipelines, artificial reservoirs) and property (buildings, agricultural land), have been the result of mass wasting processes. Landslides are generally induced when the shear stress on the slope material exceeds the material's shear strength and can be triggered by intense short-period or prolonged rainfall, earthquakes, or human activities (Nadim et al., 2006; Swiss Re, 2011a, 2011b; Varnes and IAEG, 1984). A significant degree of the damage and a considerable proportion of the human loss associated with earthquakes and storm events are caused by landslides as tragically demonstrated during major events in China in 2008 (Dai et al., 2011; Gorum et al., 2011) and Brazil in 2011 (Avelar et al., 2013). There is a need to improve our understanding of landslide processes, identify the mechanisms that trigger landslides, develop methods for landslide susceptibility mapping, keep historic records of landslides, and develop flexible and reliable monitoring methods. During the last decade there has been an increase in the use of remote sensing technology for mapping and monitoring of landslides. There has been a significant improvement in the spatial resolution of remote sensing technology in particular with the introduction of laser scanning (both airborne and terrestrial) (Razak et al., 2011) and unmanned aerial vehicles (UAVs) (Niethammer et al., 2012). This paper describes an image-processing workflow based on the combined use of UAVs, computer vision, and image correlation techniques for detailed monitoring of landslides, however, we first review the key remote sensing techniques used for landslide mapping moving from coarse to fine resolutions.

A wide range of spatial and temporal scales and a variety of spaceborne, airborne, or ground-based remote sensing techniques like optical sensors, thermal, LiDAR, and microwave sensors have been applied for studying landslides (Delacourt et al., 2007; van Westen et al., 2008). Earth observation methods are useful to produce detailed multi-temporal sets of images, orthophotos, and digital elevation models (DEMs). These products may provide us with insight into the flow kinematics such as flow rate, landslide expansion, and accumulation at the toe zone or retreating scarps. In addition, these new techniques allow volume calculations of the accumulated and removed material by the landslide and mapping of the topographic changes (McKean and Roering, 2004; Ventura et al., 2011). Key examples of spaceborne remote sensing techniques based on optical and RADAR sensors for landslide studies are reviewed in Guzzetti et al. (2012), Joyce et al. (2009), and Metternicht et al. (2005).

Detailed three-dimensional (3D) information on the land surface can be obtained with laser scanning techniques, such as airborne LiDAR and terrestrial laser scanning (TLS) (Glenn et al., 2006; McKean and Roering, 2004; Razak et al., 2011; Ventura et al., 2011). Razak et al. (2011) succeeded in mapping scars and escarpments of a landslide and its dynamics under forests from a time series of very high resolution airborne LiDAR (140 points per m^2). TLS is a ground-based laser scanning technique to measure the position and dimension of objects in 3D space. Landslide movements can be detected by comparing sequential scans; for example, Abellan et al. (2009, 2010) successfully used TLS to quantify volumes and frequencies of rockfall from landslides and steep cliffs.

Dewitte et al. (2008) used stereo photogrammetry applied to historical aerial photographs to produce DEMs and in combination with a LiDAR DEM they tracked small landslide displacements. Fiorucci et al. (2011) analysed time series of airborne and spaceborne optical images and used this data set to prove the seasonal behaviour of landslide activity and the relation with rainfall events in central Italy. Recently, Travelletti et al. (2012) successfully applied image correlation techniques on ground-based images to calculate the

displacements of the Super-Sauze landslide in the French Alps.

Although spaceborne and airborne remote sensing techniques are widely used for studying landslides, these Earth observation methods are not as flexible as the novel remote sensing platform of unmanned aerial vehicles (UAVs). Spaceborne and airborne image acquisitions require thorough planning and might be hampered by unfavourable weather conditions or other campaigns with higher priorities. Recent developments in UAV technology provide exciting new opportunities for ultra-high resolution (1–20 cm resolution) mapping and monitoring of the environment. The key advantages of UAVs for environmental remote sensing include their superior spatial resolution, the capacity to fly on-demand at critical times, and their capability of carrying multiple sensors. UAV-mounted sensors are ideal tools to map and monitor dynamic features at the Earth surface, such as river channel vegetation (Dunford et al., 2009), rangeland vegetation (Laliberte and Rango, 2009; Laliberte et al., 2010, 2011), Antarctic moss beds (Lucieer et al., 2014; Turner et al., 2012), crop health status (Zarco-Tejada et al., 2011), and saltmarsh vegetation (Kelcey and Lucieer, 2012). UAVs provide a convenient remote sensing platform for landslide studies given their ability to collect ultra-high resolution imagery over terrain that is often difficult to access. Furthermore, UAV observations may bridge the gap between terrestrial observations and satellite or full-scale airborne observations. UAV-mounted sensors are not new, but advances in technology like small, lightweight UAVs capable of carrying a considerable payload, lightweight cameras, GPS, and autopilots combined with advanced software allowing accurate geocoding of imagery have given a boost to these developments (Dunford et al., 2009; Neitzel and Klonowski, 2011).

In addition to UAV technology, recent advances in photogrammetric image processing and computer vision have resulted in a technique known as Structure from Motion (SfM) (Snavely et al., 2008). Highly detailed 3D models can be obtained from overlapping multi-view photography with SfM algorithms. Even though the technique was originally designed for 3D reconstructions of building facades (e.g. Furukawa and Ponce, 2010; Snavely et al., 2008) and archaeological sites (e.g. Verhoeven, 2011), more recently the technique has been successfully applied in Earth sciences for flexible and cost-effective mapping of a range of object scales ranging from individual rock samples to entire landscapes. James and Robson (2012) demonstrated the application of SfM in three case studies: a geological rock sample (0.1 m sample size), a coastal cliff (50 m size), and a crater landscape (1600 m size). Westoby et al. (2012) used SfM techniques to map the 3D structure of a steep alpine hill slope and demonstrated that the SfM-derived elevation measurements were within 0.1 m of a TLS scan. Fonstad et al. (2013) also showed accurate SfM results for geomorphological mapping in comparison with on-ground GPS (<0.1 m error in X, Y, and Z) and airborne LiDAR surveys.

In combination with UAV technology, SfM can provide a cost-effective and efficient means to acquire dense and accurate 3D data of the Earth surface. d'Oleire-Oltmanns et al. (2012) demonstrated the use of a small fixed-wing UAV for mapping and monitoring soil erosion in Morocco. Flying at 70 m above ground level (AGL) they achieved accuracies better than 3 cm using SfM techniques. Harwin and Lucieer (2012) achieved accuracies between 2.5 and 4 cm when mapping a coastal cliff with a multi-rotor UAV and an SfM workflow. Turner et al. (2012) and Lucieer et al. (2014) used a multi-rotor UAV and SfM workflow to derive DEMs and orthomosaics of Antarctic moss beds achieving absolute geometric accuracies of 4 cm compared with DGPS ground control. Carvajal et al. (2011) demonstrated the use of a small quadcopter UAV for surveying landslides in a road embankment. They achieved

Figure 1. Overview of the Home Hill landslide located in southern Tasmania. The height of the scarp (head wall) is 4–5 m.

planimetric accuracies of ~0.5 m and a height accuracy of 0.11 m. The application of UAVs and SfM for landslide mapping was elegantly demonstrated by Niethammer et al. (2010, 2012) who employed a quadcopter UAV to acquire aerial photography and generated DSMs and orthomosaics of the Super-Sauze landslide in southern France based on photogrammetric techniques achieving geometric accuracies of around 0.5 m. Niethammer et al. (2012) also used multi-temporal UAV orthomosaics to visually identify and quantify changes in the landslide. Our study aims to build on this work by automating the change detection process with image correlation techniques.

The work by Niethammer et al. (2012) and Travelletti et al. (2012) inspired us to combine UAV SfM mapping of landslides with semi-automated image correlation analysis to quantify landslide dynamics. In this paper, we illustrate a workflow showing how UAV-acquired images can be processed into high resolution DEMs and orthomosaics used for quantifying landslide dynamics based on multi-temporal image correlation. The objectives of this paper are:

- to illustrate how time series of digital photographs acquired over an active landslide by a flexible and cost-effective UAV can be converted into very detailed 3D point clouds, DEMs, and orthomosaics using on-board GPS and field DGPS observations;
- to show how these orthomosaics and DEM-derived products can be used to quantify and map the dynamics of a landslide.

II Research design and methods

1 Study area

To demonstrate the SfM and image correlation techniques described in this study we selected an active rotational slump as the main trial site. The Home Hill landslide is located on the northern flanks of the Huon valley in southern Tasmania approximately 35 km southwest of Hobart at an elevation of approximately 80 m above sea level (Figures 1 and 2). At the top of the slope the landslide is a rotational earth slide and downhill it develops into an earth flow. The dimensions of the landslide are approximately 125 m by 60 m and it has developed in strongly weathered, layered fine colluviums which are remains of underlying Permian mudstone and siltstone estimated to be 4–5 m deep (McIntosh et al., 2009). Land use is pasturage and no trees are present on the

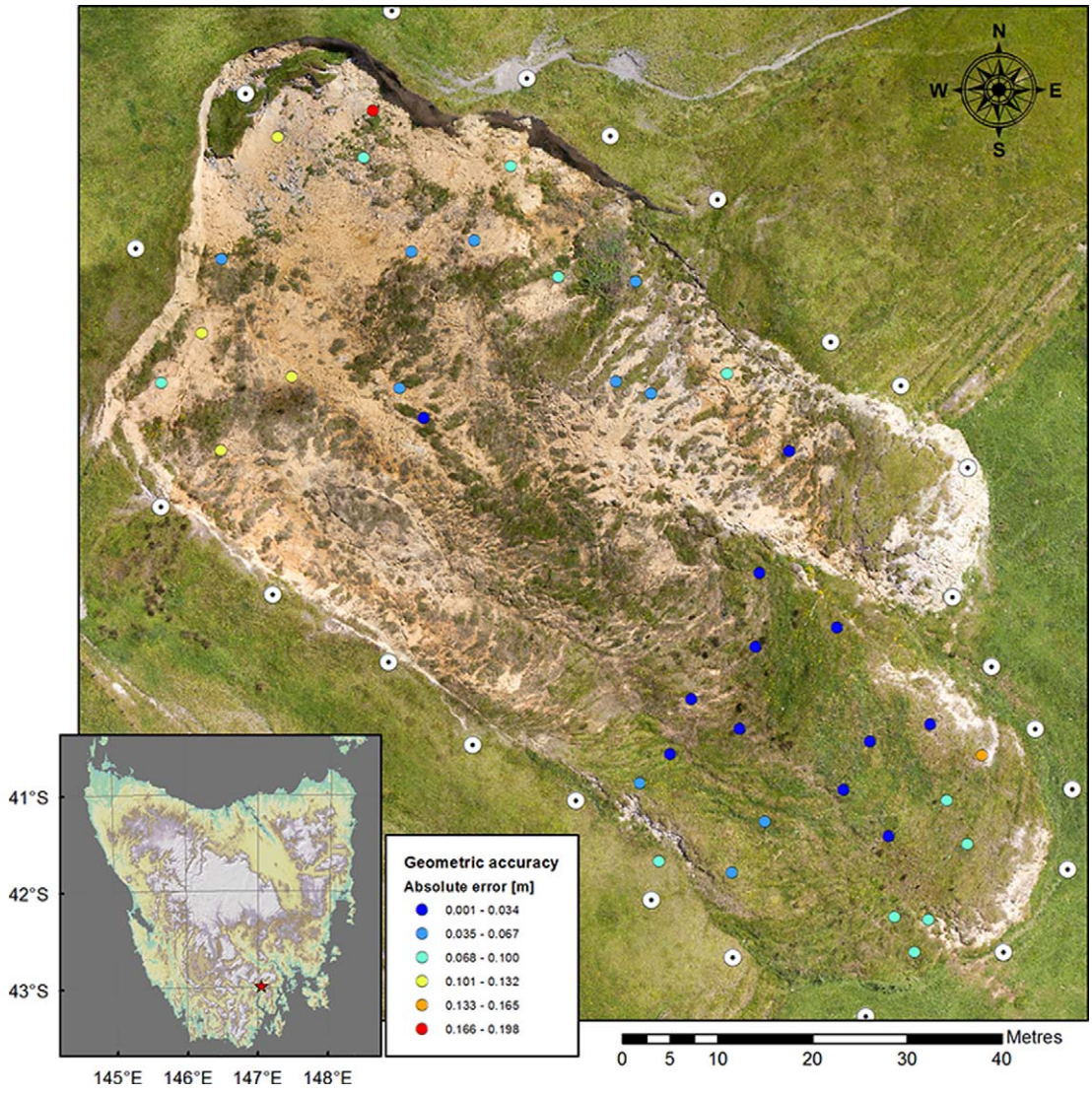

Figure 2. Location map and orthophoto mosaic acquired by UAV of the Home Hill landslide in Tasmania on 19 July 2011. The locations of the 24 GCPs used for the SfM bundle adjustment are shown as white disks. The 39 GPS samples used for independent accuracy assessment are shown as smaller coloured circles depicting their horizontal errors.

slope. The landslide developed in 1996 and is still active. Field and aerial surveys revealed that the main scarp developed 5 m backwards and the northern toe extended approximately 4–5 m between 19 July 2011 and 10 November 2011. The surface of the slide also showed significant dynamics including downward shifting movements and tumbling and overturning of blocks. Figure 2 shows an aerial photograph (orthomosaic) of the landslide acquired by our UAV. The main scarp is clearly visible with a vertical wall of approximately 4–5 m. Two landslide toes are visible from which the small northern toe is most active.

Figure 3. The remote controlled UAV OktoKopter equipped with digital camera and GPS.

2 UAV aerial survey

Airborne digital photographs over the landslide were acquired on two dates, 19 July 2011 and 10 November 2011, using a small multi-rotor UAV. An OktoKopter is a multi-rotor helicopter with eight rotors, also classified as a micro-UAV. Our OktoKopter (Figure 3) is approximately 80 cm in diameter and has a total take-off weight of 3 kg. It is equipped with an autopilot and navigation-grade GPS receiver. It carries a standard Canon 550D DSLR camera on a motion-compensated gimbal mount. A Canon 18–55 mm f3.5–5.6 IS lens was used given its low weight. The lens was fixed to a focal length of 18 mm during flight and operated in autofocus mode. The camera was set to shutter priority with a fast shutter speed of 1/1200 to reduce motion blur. The ISO was set to 200 to limit noise in the photographs and the aperture was automatically adjusted by the camera to achieve the desired shutter speed, but generally large apertures were selected with f-values around 3.5. The camera was triggered by the flight controller every ~1.5 seconds by a custom-made trigger cable. The UAV flight path was recorded by the on-board GPS logging at 1 Hz. The average flying height was 40 m above ground level (AGL) guided by the autopilot. Each 18 megapixel photograph covered approximately 50×34 m on the ground resulting in 1 cm resolution imagery. On 19 July 2011 238 UAV photographs were collected, and on 10 November 2011 224 photographs were collected for processing. Despite the impact of relatively strong wind gusts (~25 knots on 10 November 2011) on the UAV platform, we show here that it is possible to produce accurate image products. We had overcast and diffuse sunlight on 19 July 2011 and scattered clouds with varying light conditions on 10 November 2011. A visual selection of the photographs was made on the basis of quality, viewing angle, and overlap for further processing, i.e. blurred images and under- or overexposed images were removed from further analyses, resulting in 98 photographs for the July flight and 118 photographs for the November flight. During UAV data acquisition 24 circular, aluminium reference disks with a 22 cm diameter, bright orange rim, and a clearly defined centroid (visible as a single black pixel in the images) were laid out around the landslide for georeferencing purposes (GCPs) for both UAV survey dates. Another 39 aluminium orange disks with a 10 cm diameter were spread out across the landslide for accuracy assessment purposes on the 19 July 2011 survey. The disks were manually identified in the UAV imagery for georeferencing and validation. The disk locations were measured in the field directly after UAV image acquisition using a Leica Viva GNSS system in dual-frequency real-time kinematic mode, providing centimetre positional and height accuracies (2–4 cm).

3 Structure from Motion (SfM) for 3D model generation

The SfM process starts by acquiring photographs of the object of interest with sufficient overlap (e.g. 80–90%) from multiple positions and/or angles. Based on advances in image feature recognition, such as the scale invariant feature transform (SIFT) (Lowe, 2004), characteristic image objects can be automatically

detected, described, and matched between photographs. A bundle block adjustment is then performed on the matched features to identify the 3D position and orientation of the cameras, and the XYZ location of each feature in the photographs resulting in a sparse 3D point cloud (Snavely et al., 2008; Triggs et al., 2000). A subsequent densification technique can then be applied to derive very dense 3D models using multi-view stereopsis (MVS) or depth mapping techniques (Campbell et al., 2008; Furukawa and Ponce, 2009, 2010). The use of ground control points (GCPs) and/or incorporation of camera GPS locations allows georeferencing of the 3D model in a real-world coordinate system. Finally, the model can be exported to a grid-based DEM and orthophoto mosaics (orthomosaics) can be derived based on the projected and blended photographs.

In this study, we adopted the SfM workflow as implemented in the commercial software package Agisoft PhotoScan Professional version 0.85.2 The specific algorithms implemented in Photoscan are not detailed in the manual, however, a description of the SfM procedure in Photoscan and commonly used parameters are described in Verhoeven (2011) and Doneus et al. (2011). The algorithms in Photoscan are highly optimized for the graphics processing unit (GPU). We followed the SfM workflow described below.

Image preparation. After visual pre-selection, coordinates were assigned to the UAV-acquired images. GPS points registered on-board the UAV were linked to the photographs using the time settings of the digital camera, which was synchronized with GPS time immediately before the UAV flight. The technique takes the 1 Hz sampled GPS points and interpolates the photograph location (coordinates) from the UAV flight path. For this process we used the GeoSetter freeware (www.GeoSetter.de) to write the UAV GPS coordinates to the corresponding JPEG EXIF headers, i.e. geotagging. Lens distortion parameters were calculated using an on-screen lens calibration procedure implemented in the AgiSoft lens calibration software, which models the focal length, principal point coordinates, and radial and tangential distortion coefficients using Brown's distortion model. We acknowledge that these lens distortion coefficients vary for different focus distances. We therefore used the coefficients as an initial estimate, but we did not fix the coefficients in the bundle adjustment.

Image matching and bundle block adjustment. We imported the pre-selected geotagged photographs into Photoscan. The photographs were aligned with the accuracy setting set to high with the pair pre-selection based on image GPS coordinates as stored in the JPEG EXIF headers. Attaching GPS coordinates to the photographs speeds up the feature-matching process as Photoscan can pre-position the images and only match features in photographs that overlap. Feature matching is followed by a bundle block adjustment. Obvious outliers were deleted from the sparse point cloud to reduce reconstruction errors.

Dense geometry reconstruction and inclusion of GCPs. A dense 3D model was built using 'height field' as the object type, the geometry type was set to smooth, and the target quality was set to medium with a face count limited to 10 million faces (i.e. number of triangles). This resulted in a 3D model that could be used to manually identify the 24 GCP disks in the model and the corresponding photographs. The 3D model can be used to 'roughly' position GCP markers in the centroid of the disks after which the exact position of the markers can be fine-tuned in the individual photographs. Based on the field-measured GPS coordinates of the GCPs, the bundle adjustment was recalculated with estimated accuracy settings of the camera GPS coordinates set to 10 m and the ground GCPs set to 2 cm. Photoscan uses both sets of GPS coordinates with

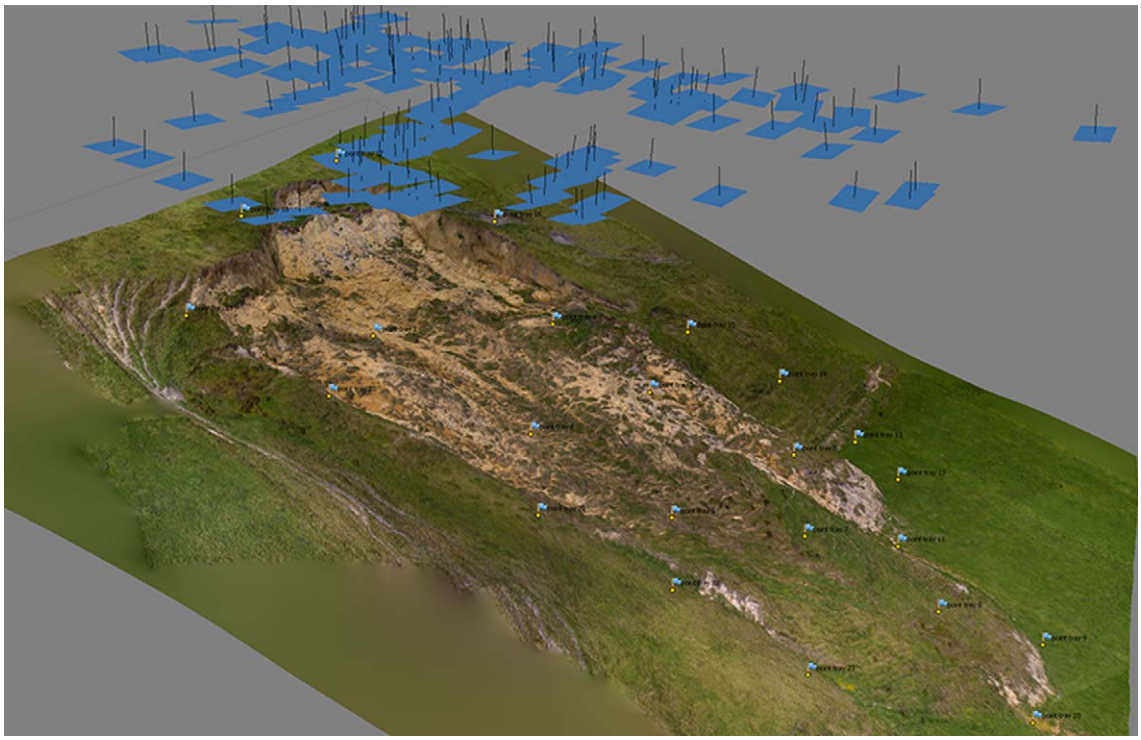

Figure 4. Perspective view of the texture-mapped 3D surface acquired on 10 November 2011. The blue squares over the landslide show the camera positions and orientations during image acquisition by the UAV. The numbered flags on the landslide show the positions of the ground control points used for the bundle adjustment.

their estimated accuracy to fine-tune the bundle adjustment. Residuals for the GCPs were calculated as an initial indication of the geometric accuracy of the model. Based on the updated bundle adjustment, the dense 3D geometry was recomputed with the target quality set to high, again with a target face count for the model of 10 million.

Texture mapping and export of DEM and orthophoto mosaic. Texture mapping can add photographic detail to the 3D surface based on the original images. An example of a texture-mapped 3D model of the Home Hill landslide based on the 19 July 2011 UAV survey is shown in Figure 4. Finally, a DEM was exported in the GeoTIFF format at 1 cm resolution. An orthophoto mosaic was also exported at 1 cm resolution. The orthomosaic is generated by correcting the individual photographs for relief distortions and projecting them onto a planimetric surface with a real-world coordinate system (for our study area: Geocentric Datum of Australia 1994 (GDA94) UTM Zone 55 S). These photographs were blended into a single orthomosaic at 1 cm spatial resolution. For some analyses we worked at this high resolution of 1 cm; for other analyses we worked at a reduced resolution of 10 cm, as further explained below. Subsequent accuracy assessment and spatial analyses were carried out in IDL/ENVI 4.8[3] and ArcGIS 10.0 (ESRI).

Accuracy assessment. The accuracy of the models was assessed in two different ways: (1) the XYZ

residuals for the 24 GCP disks were calculated in Photoscan as part of the bundle adjustment and model generation process; (2) an independent validation was carried out with the 39 smaller disks for the 19 July 2011 UAV survey. These disks were identified in the orthomosaic and the error in X and Y measured. The difference in height was measured on the DEM. Summary statistics, such as minimum, maximum, mean error, standard deviation, and root mean squared error (RMSE), were calculated to quantify geometric accuracies.

3 Visual interpretation of surface dynamics

The dynamics of the landslide between two acquisition dates were visually investigated by overlaying two orthomosaics in RGB combinations in an image-processing system (ENVI). One band of the first image, for example green for 19 July 2011, was assigned to the red channel, and the green band of the second image (10 November 2011) was assigned to the green and blue channels. Such colour combinations allow easy recognition of the displacements on screen. Next, using a measuring tool, the displacement magnitudes (in metres) and the displacement directions were mapped for clearly identifiable features on the landslide. The measurements include the retreat of the main scarp, the extension of the two toes of the landslide, and the displacements of identifiable features on the surface of the slide such as circular patches of grass and ground lobes.

4 Image correlation and displacements measurements

After precise co-registration of the UAV orthomosaics, the horizontal dynamics of the landslide were determined using an advanced image correlation method developed by LePrince et al. (2007, 2008). The method is referred to as COSI-Corr: Co-registration of Optically Sensed Images and Correlation (Ayoub et al., 2009).[4] It considers two single-band images of any source, such as optical satellite images acquired by ASTER (Herman et al., 2011) and by SPOT (Leprince et al., 2007) or DEMs derived from SRTM or ASTER (Scherler et al., 2008). COSI-Corr can also work with orthorectified aerial photography, such as our UAV orthomosaics. Since the algorithm works on single-band images, the multi-band RGB image must be converted to a single-band image. In this study, we evaluated the following single-band images for displacement mapping: the individual colour bands (red, green and blue); the first and second principal component images (the third PC image was too noisy for analysis); colour transformed images – hue, saturation and value (i.e. luminosity grey-scaling) images; the average DN-value in the three RGB bands; and a DEM-derived product – the shaded relief map. The hillshade operator was applied with a sun elevation of 45° and an azimuth of 315°. These illumination conditions are representative of the solar position during a typical summer afternoon. The azimuth of the light source corresponds to the general northwest to southeast direction of the landslide. The artificial lighting in the hillshade operator should therefore highlight the main terrain features, such as lobes and fissures in the main flow direction of the landslide.

COSI-Corr uses an image kernel to compute the correlation between the two images. Two correlation algorithms are proposed by LePrince et al. (2007). The first is a frequency correlation method computing the relative displacement between the pair of images retrieved from a Fourier transform. The second is a statistical correlation method defined as the absolute value of the correlation coefficient of a patch in one image and the corresponding patch in the other image. The estimated misregistration or displacement, expressed in pixels, is found from quadratic approximation, separately in each x and y dimension, of the maximum of the correlation matrix. A typical correlation analysis is performed using window sizes of 128 down to 32 pixels, steps of 4 pixels between adjacent correlations, and a search radius of a few metres,

but this requires heuristic fine tuning. The input images should be co-registered as accurately as possible as the correlation algorithm is sensitive to image misregistration errors. In addition, image noise due to striping and sensor noise, but also illumination differences (e.g. caused by clouds and shade), will have a deteriorating effect on the displacement analysis.

The displacement algorithm in COSI-Corr requires a number of initial settings (Ayoub et al., 2009): (1) window size – the size in pixels of the patches that will be correlated in x and y direction; (2) step – determines the step in x and y direction in pixels between two sliding windows; (3) search range – indicates the maximum distance in the x and y direction in pixels where the displacements to measure are to be searched. Appropriate setting of these initial values for the displacement algorithm requires a priori knowledge of the size of displacements. The correlation algorithm results in three output images. The first two images provide the 2D displacement field computed from the image correlation containing the east–west displacement (east positive) and the north–south displacements (south positive) both expressed in metres. The ground displacement (direction and distance) is computed by combining these two images by the square root of the sum of the squared displacements. The third image shows the spatial distribution of the signal-to-noise ratio allowing assessment of the quality of the computed displacement. A detailed description of the algorithm is available in LePrince et al. (2007) or from http://www.tectonics.caltech.edu. The software is implemented in IDL and available in the image-processing software ENVI. Finally, the computed displacement can be visualized using vector fields illustrating the direction and the magnitude of the displacements.

IV Results

In this section we present the results of the visual interpretation of the landslide displacements based on comparison of orthomosaics, and we present the obtained accuracy of the orthorectification and the DEM production and the Home Hill landslide deformation calculations. Finally, we present the displacement results derived with COSI-Corr.

1 Visual interpretation of orthomosaics

Photoscan was run on a PC with an Intel Xeon E31240 3.3Ghz CPU with 32 GB RAM and an NVIDIA GeForce GTX590 graphics card running Windows7 64-bit. The computing time required for the SfM workflow for a single acquisition date was as follows: (1) image feature detection and matching: 75 minutes; (2) creation of dense 3D geometry: 65 minutes; (3) manual/visual identification of GCPs: $\sim$2 hours; (4) re-creation of dense 3D model: 65 minutes; and (5) creation of DEM and orthophoto: 30 minutes. The 3D models contained 5 million vertices over a 1 ha area, which corresponds to 500 points per m^2. The displacements on and around the landslide and the expansion of the landslide were mapped by visual interpretation of the set of orthomosaics. Figure 5 shows the orthomosaic of 19 July 2011 in red and the orthomosaic of 10 November 2011 in green and blue. Overlaid onto the orthomosaics, vectors indicate the direction and size of movement. The displacements of material on the landslide are not equally distributed over the slide but displacements are irregular and greatly differ from one location to another. The northern part of the main scarp (D) retreated around 5.5 m in less than four months. The northern smaller toe (C) was most active and expanded 3–4 m at the toe in various directions. The failure of the main scarp and the extension of the toe were most likely triggered by an active chunk in the central northern part. This moving chunk removed the support of the main scarp and led to the further collapse and retreat of the main scarp and also triggered the extension of the toe. The southern part of the main scarp retreated far less (around

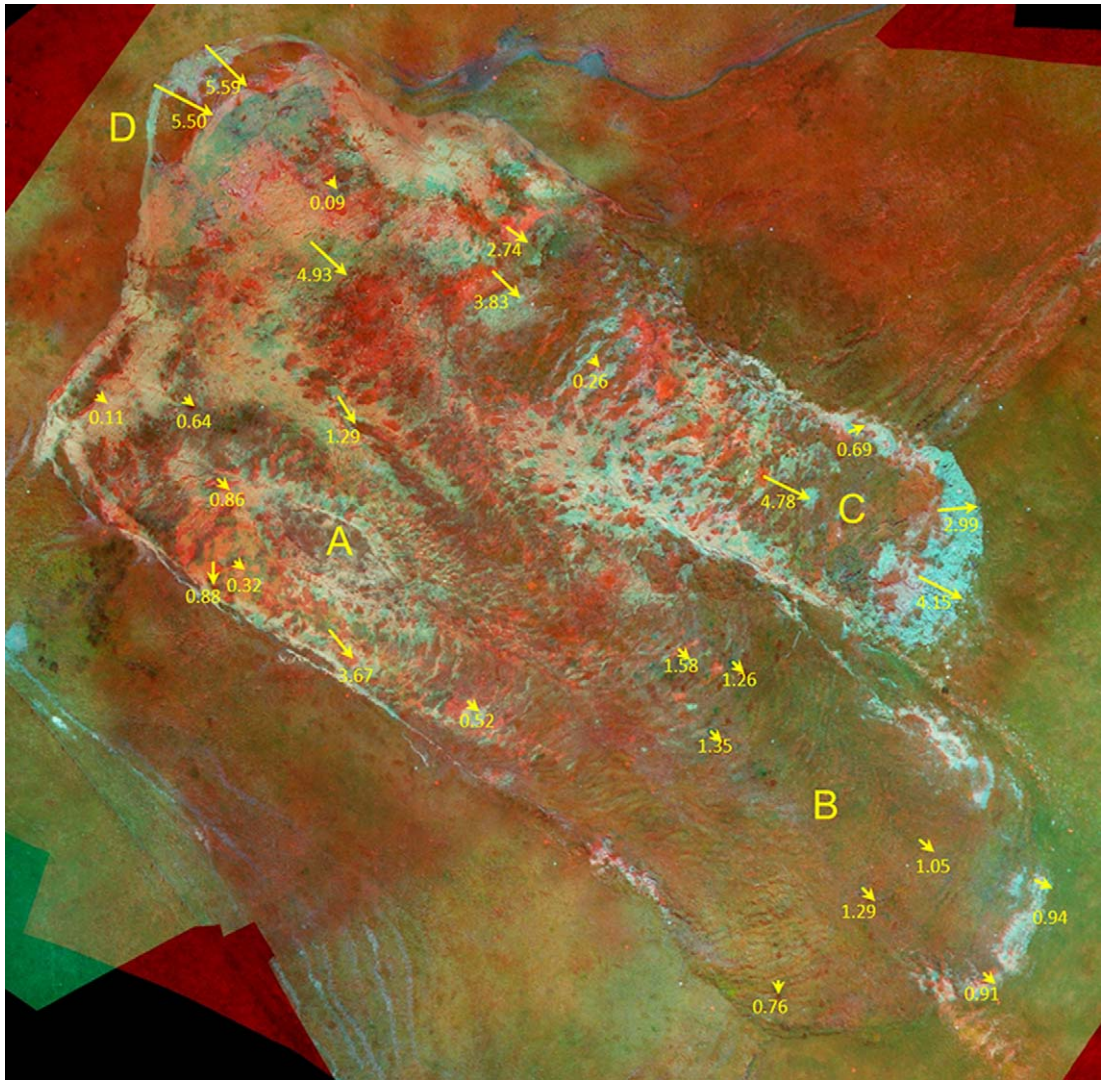

Figure 5. Multi-temporal colour combination of orthomosaics of the Home Hill landslide with the 19 July 2011 orthomosaic in red and the 10 November 2011 orthomosaic in green and blue. The vectors and numbers in yellow indicate the displacement (distance and direction) of the landslide features mapped by visual interpretation.

0.1 m) and the large, southern toe (B) expanded around between 0.9 m and 1.6 m. It is remarkable that the oval portion (16 × 5 m) of ground in the southern part of the main body of the slide (A) did not move at all, while all around this area the material moved over considerable distances as shown by the arrows in Figure 5. The visual interpretations presented here yielded a basis to validate the automatic deformation calculations presented in the following sections.

2 Orthomosaics and DEMs

The accuracy of the 3D models was assessed based on the residuals of the bundle adjustment. Summary statistics of the 24 GCPs used as

Table 1. Evaluation of the residuals for the 24 GCPs used for georeferencing of the 3D models.

Date	RMSE X (cm)	RMSE Y (cm)	RMSE Z (cm)	Total RMSE (cm)
19 July 2011	2.4	2.3	1.4	3.6
10 Nov 2011	3.8	2.7	6.3	7.8

Table 2. Evaluation of the geometric accuracy of the 1 cm orthomosaic of 19 July 2011 using 39 independent DGPS field reference discs.

Orthomosaic 19 July 2011	Average (cm)	Minimum (cm)	Maximum (cm)	Stand. dev. (cm)	RMSE (cm)
Horizontal accuracy	6.1	0.1	19.8	4.1	7.4
Vertical accuracy	0.6	−11.2	11.8	6.2	6.2

Table 3. Evaluation of the relative elevation accuracy of the two 1 cm resolution DEMs of 19 July 2011 and 10 November 2011 by analysing the difference between the two DEMs and considering static, unchanged areas outside the landslide area.

OrthoDEM difference 9 July 2011 to 10 Nov 2011	Average (cm)	Absolute minimum (cm)	Absolute maximum (cm)	Stand. dev. (cm)	Number of pixels
Evaluation of invariant areas	1.7	0.0	23.1	4.1	205,000

ground control are provided in Table 1. The overall RMSE for the 19 July 2011 survey was 3.6 cm and the RMSE for the 10 November 2011 survey was 7.8 cm. The larger errors for the 10 November 2011 survey could be an indication of the influence of strong wind gusts and suboptimal flight path patterns.

An independent verification of geometric accuracies was carried out on 39 additional GCP disks for the 19 July 2011 survey. A summary of the horizontal and vertical errors is provided in Table 2 and the spatial distribution of the horizontal errors is shown in Figure 2. The overall horizontal RMSE was 7.4 cm and the vertical RMSE 6.2 cm. For the 10 November 2011 data acquisition such a reference set of additional disks was not available.

An additional accuracy assessment was carried out on the 1 cm DEMs by computing the vertical offset of the DEMs acquired on 19 July 2011 and 10 November 2011 for several static areas. Four polygons, each comprising approximately 50,000 pixels, were digitized on the difference map at locations away from the landslide area (in the northwest, northeast, southwest, and southeast corners). These areas were expected to be static and unchanged although field observations revealed that irregular grazing took place, which will have an impact on the vertical accuracy of the multitemporal DEMs. The absolute mean difference between the two DEMs for these four static polygons is 1.7 cm with a standard deviation of 4.1 cm as shown in Table 3.

Figure 6 shows a difference map between the 1 cm DEMs of 19 July 2011 and 10 November 2011. Red and blue colours indicate large volume displacements, and yellow and green colours indicate limited volume change and displacements. Visual inspection of this difference map clearly illustrates the changes that occurred between the two acquisition dates. The main scarp, the two flows, and the movement of the two toes are clearly visible in

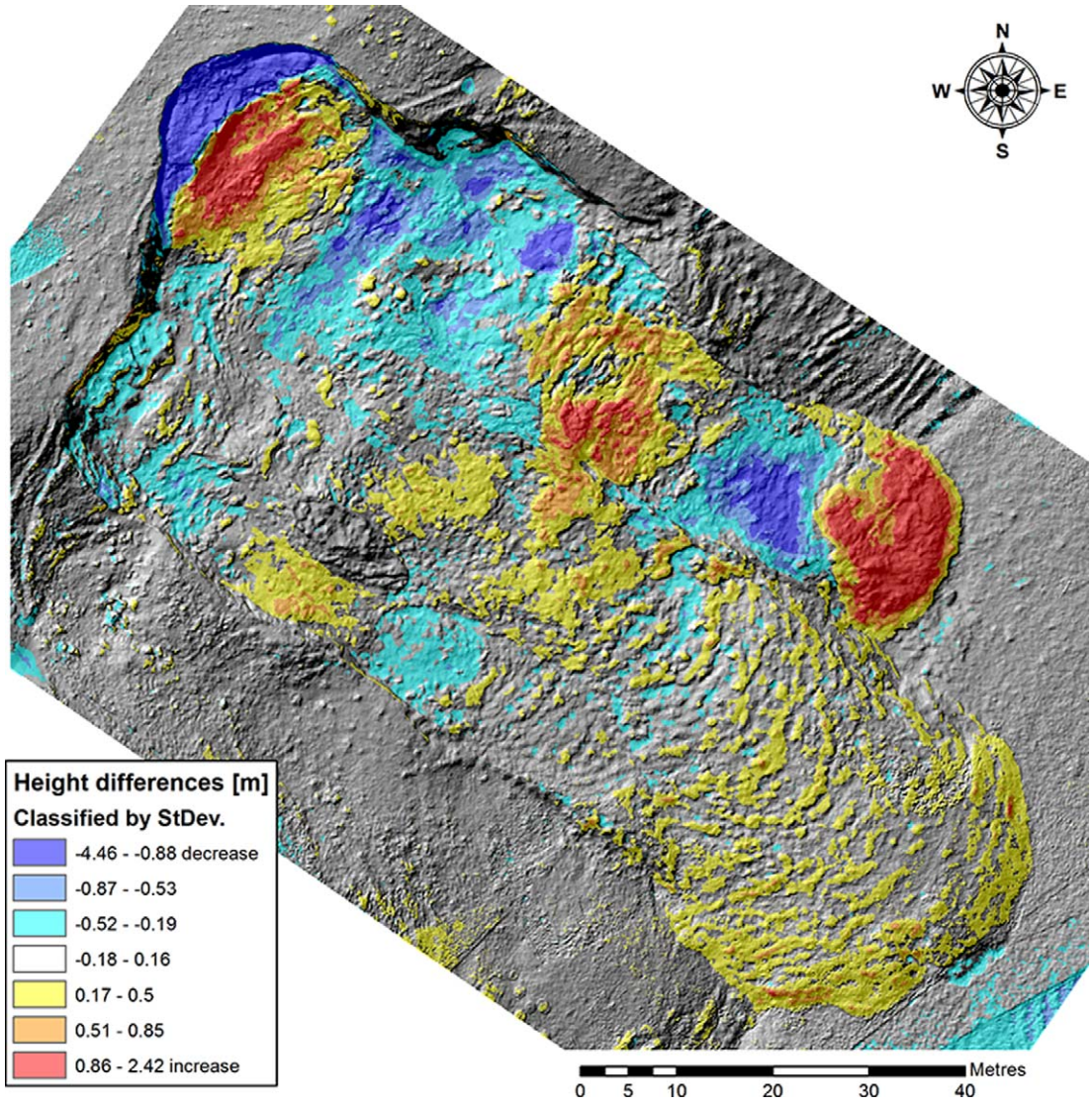

Figure 6. Difference between the 1 cm DEMs of 19 July 2011 and 10 November 2011 illustrating the surface changes and as such the dynamics of the landslide. Note the significant retreat of the main scarp and the expansion of the toes.

the DEMs and difference image. Furthermore, the difference image illustrates that material is removed from the northern, central flank of the landslide and has contributed to the movement of the small toe. Figure 6 also illustrates the relatively small vertical displacements of the large toe ($\sim$0.5 m) and the general shape of these movements as concentric half-circles. The static oval shaped feature is also clearly visible in this difference image.

3 Deformation computations using COSI-Corr

The relative displacements between two image acquisition dates were computed using the

Table 4. Displacements in metres of selected Home Hill landslide features computed using the algorithm COSI-Corr (Leprince et al., 2007). Total displacements between image dates and their standard deviation are given. The average daily displacement between image acquisition dates is presented in brackets.

Image acquisition dates	Large toe	Small toe
19 July 2011 to 10 Nov 2011 (123 days)	127 cm $\pm$ 14 (1.0 cm/day)	468 cm $\pm$ 17 (3.8 cm/day)

image correlation method implemented in the COSI-Corr package. All images were resampled to 10 cm resolution for better performance of COSI-Corr. At the full resolution of 1 cm the features between the images were too different for reliable image correlation; hence a reduction in resolution was required. The use of the shaded relief map to compute displacements between two image dates provided the best results and was superior over all the other single-band images. The statistical correlation method yielded the best results compared with the visual interpretation of the displacements on the landslides. As described in section II.5, the settings of window size, step size, and search radius requires heuristic fine tuning and some a priori knowledge of the deformations derived, e.g. from visual interpretation of the photographs or field observations. The best parameter settings for the statistical correlator for deformation mapping were a window size of 64 pixels, a step size of 8 pixels and a search radius of 50 pixels (5 m). Table 4 shows the displacements (and standard deviations) of the two toes of Home Hill landslide computed by COSI-Corr for the two UAV survey dates. Between brackets the average displacement per day is presented. Table 4 provides an estimate of the rate of displacement per day but it should of course be noted that the displacement often occurs stepwise in surges and that the time between the different image acquisitions dates does not allow a very detailed assessment of the deformation velocity. It is therefore only possible to present an average deformation velocity per day.

Figure 7 shows the results of the image correlation algorithm between 19 July 2011 and 10 November 2011 as vector fields plotted on a displacements magnitude map. These results were obtained using the shaded relief single images of the two dates, the statistical correlator of COSI-Corr, and a window size of 8–64 pixels with a search radius of 5 m. The vector field of Figure 7 is computed by combining the east–west and north–south displacement. The white vectors indicate the computed direction of movement and the length of the vectors indicates the relative displacement. The computed displacements range from 0 to 6.9 m with a standard deviation of 1.49 m. The figure clearly shows the high dynamics of the small, northern toe (4–7 m) and the slower but steady movement of the large, southern toe (1–2 m). At the edges of the toes, near the scarps and on the main body of the slide the computed displacements show a less clear image. The movements are more complex, edges are steep and rotational movements probably make it difficult for the image correlation algorithm to produce reliable results. The static oval-shaped block of 16×5 m in the southern part of the main body of the slide is very well identified by the algorithm. The longitudinal displacements for the central parts of the two toes are accurately computed (based on visual validation of clearly identifiable features). The lateral flow of material at the end of the toes is also appropriately represented. Displacements of vegetation patches and chunks of ground material are correctly identified. At the active part of the scarp the algorithm suggests a northwest movement, however, the chunk of collapsed material moves southeast in reality. Some vectors are computed for the static grass area outside the landslide area and so far no explanation for these suggested movements was found.

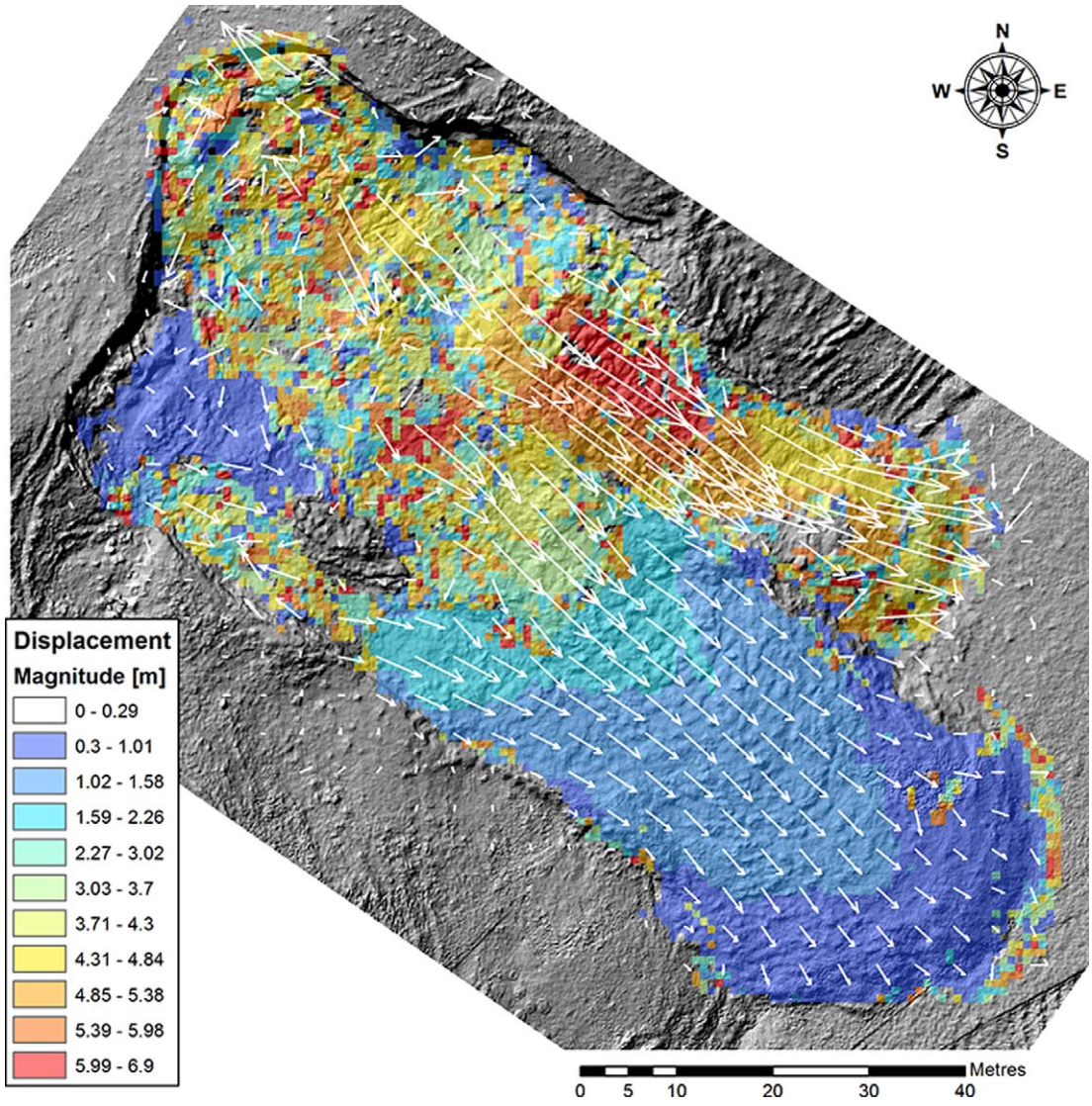

Figure 7. Displacement of the Home Hill landslide between 19 July 2011 and 10 November 2011 using the COSI-Corr algorithm. The white vectors indicate displacement directions and the coloured layer illustrate the combined magnitude of displacements in the N–S and E–W directions.

V Discussion

This study presents a detailed and accurate mapping and monitoring workflow for landslides based on UAV imagery, SfM algorithms, and image correlation methods for displacement mapping. Successful monitoring of landslides requires that the set of overlapping UAV images (generally hundreds) is processed by structure from motion (SfM) and multi-view stereopsis (MVS) algorithms, resulting in accurate DEMs and orthomosaics. A number of sources of uncertainty can be identified. Different illumination conditions during image acquisition are a source of uncertainty, including direction of solar illumination and shadowing, diffuse light

under overcast conditions or direct sunlight resulting in different image contrast. Weather conditions with scattered clouds and resulting sharp and dark shadows makes the process even more difficult. Differences in illumination conditions in addition to differences in vegetation condition (e.g. lush spring grass versus short winter grass) between the acquisition dates can hamper the COSI-Corr algorithm to identify matching features between images acquired under different lighting conditions. Since the algorithm searches for similar surface patterns in a specified search radius, clouds and cloud shadows have an impact on these patterns and hence an impact on the displacement vector computation.

The evaluation of the obtained accuracy of the orthomosaics and DEMs is not an easy task. We recommend the use of two sets of clearly visible reference markers (GCPs) randomly placed on and around the landslide with accurate XYZ coordinates measured by DGPS or more accurate means (e.g. Totalstation). One set of GCPs can then be used for the orthorectification process and the second set is useful for accuracy assessment. James and Robson (2012) give a minimum relative precision ratio of 1:1000 (coordinate precision: viewing distance) for SfM projects using Bundler and PMVS2. For a flying height of ~40 m AGL this rule should result in a coordinate precision of 4 cm. The RMSE values in Tables 1 and 2 show that our accuracy results are close, but slightly worse, compared to this theoretical precision. Harwin and Lucieer (2012) achieved absolute accuracies of 2.5–4 cm, however, their study also included oblique UAV photography and photography from lower flight runs.

The displacement algorithm uses pattern matching on the surface of the landslide to determine the direction and the size of the movements. Input in this algorithm is a single image band. From the various inputs we used, the shaded relief map, derived from the DEM, gave the best results. Shaded relief simulates the relative shadowing on the topography based on a solar azimuth of 315° and solar elevation of 45°. The reason that shaded relief is superior over the other single-band images is probably because shaded relief enhances the surface patterns on the landslide. In future research we plan to experiment with other DEM derivatives such as slope and convexity, which are independent of illumination settings. Herman et al. (2011) used COSI-Corr to quantify the displacements of glaciers and they found that the algorithm is sensitive to the initial settings of window size, step size, and search range. These a priori settings will hamper a fully automated computation of displacement calculations.

The displacement algorithm proved to work well as long as the displacements of the landslide are horizontal and the landslide surface patterns remain at the surface during displacement. As soon as rotational and revolving displacements take place and surface features of the landslide are buried, the surface patterns are lost and COSI-Corr is unable to find correlated surface patterns.

The image change analysis showed that the period between 19 July 2011 and 10 November 2011 was an active period for landslide movements. The triggering mechanism for the active period was most likely the rainfall. The year 2011 was an exceptionally wet year with 950 mm of rainfall (station Kingston, Tasmania) while the long-term (1882–2011) annual average is 616 mm (Bureau of Meteorology, Australian Government[5]). Furthermore, the volume of rainfall in the month of April was extreme at 156.2 mm, while the monthly average is 51.4 mm. Two-thirds of this monthly value, i.e. 107.2 mm (Station Kingston, Tasmania), fell on 13 April 2011 (Bureau of Meteorology, Australian Government). The month of May 2011 was relatively dry (35 mm of rain) but another 76.5 mm of rain fell in just 36 hours on 8 and 9 June. These extreme rainfall events may have reactivated the Home Hill landslide, however, we did not obtain UAV imagery for the period

directly before and after these rainfall events to prove this hypothesis.

VI Conclusions

In this study, we used a UAV platform equipped with a standard digital camera and GPS to collect multi-temporal sets of very high resolution RGB images over the active Home Hill landslide in Tasmania. Structure from Motion (SfM) and multi-view stereopsis (MVS) methods were used to convert hundreds of overlapping images into 3D point clouds, DEMs and orthomosaics at 1 cm resolution. The accuracy of the SfM technique was tested with 39 DGPS ground control points resulting in a horizontal RMSE of 7.4 cm and a vertical RMSE of 6.2 cm. The multi-date DEMs were converted into shaded relief images and landslide dynamics detected using an image correlation technique. The COSI-Corr image correlation algorithm was applied to compute the horizontal displacements of landslide features showing displacement magnitudes up to 7 m. These semi-automatically mapped displacements were compared with visual interpretation of displacements. The algorithm successfully quantified movements of chunks of ground material, patches of vegetation, and the toes of the landslide, but was less successful in mapping the retreat of the main scarp. Our results indicate that a combination of UAV-based imagery and SfM algorithms for 3D surface reconstruction and subsequent image correlation on SfM products, such as DEMs and orthophotos, can be used for flexible and accurate monitoring of landslides.

Acknowledgements

The team of Dr Leprince of the California Institute of Technology (CalTech) is acknowledged for making available their COSI-Corr package. We thank the Home Hill vineyard for providing access to the landslide. We would also like to acknowledge the help of students in the KGG375 GIS: Advanced Spatial Analysis unit in semester two of 2011 with collecting GPS ground control coordinates. Finally, we thank the anonymous reviewers for their valuable suggestions and comments.

Funding

The authors are grateful for the financial support received from the Visiting Fellowship Program of the University of Tasmania (UTAS).

Notes

1. See the official Mikrokopter open source quad-rotor homepage, http://www.mikrokopter.com.
2. See 'Image-based 3D modeling', http://www.agisoft.ru.
3. See ENVI image processing software, http://www.exelisvis.com.
4. See http://www.tectonics.caltech.edu/slip_history/spot_coseis.
5. See http://www.bom.gov.au.

References

Abellan A, Calvet J, Vilaplana JM, et al. (2010) Detection and spatial prediction of rockfalls by means of terrestrial laser scanner monitoring. *Geomorphology* 119: 162–171.

Abellan A, Jaboyedoff M, Oppikofer T, et al. (2009) Detection of millimetric deformation using a terrestrial laser scanner: Experiment and application to a rockfall event. *Natural Hazards and Earth System Science* 9: 365–372.

Avelar AS, Coelho Netto AL, Lacerda WA, et al. (2013) Mechanisms of the recent catastrophic landslides in the mountainous range of Rio de Janeiro, Brazil. In: Margottini C, Canuti P, and Sassa K (eds) *Landslide Science and Practice. Volume 4: Global Environmental Change*. Berlin: Springer, 265–270.

Ayoub F, LePrince S and Keene L (2009) User's guide to COSI-Corr: Co-registration of optically sensed images and correlation. Available at: http://www.tectonics.caltech.edu/slip_history/spot_coseis/pdf_files/cosi-corr_guide.pdf.

Campbell NDF, Vogiatzis G, Hern C, et al. (2008) Using multiple hypotheses to improve depth-maps for multi-view stereo. In: *Computer Vision – ECCV* 2008, Part I, Berlin: Springer, 766–779.

Carvajal F, Agüera F and Pérez M (2011) Surveying a landslide in a road embankment using unmanned aerial vehicle photogrammetry. International Conference on Unmanned Aerial Vehicle in Geomatics (UAV-g),

14–16 September, Zurich. *International Archives of the Photogrammetry, Remote Sensing and Spatial Information Sciences* XXXVIII-1/C22: 201–206.

Dai FC, Xu C, Yao X, et al. (2011) Spatial distribution of landslides triggered by the 2008 MS 8.0 Eenchuan earthquake, China. *Journal of Asian Earth Sciences* 40: 883–895.

Delacourt C, Allemand P, Berthier E, et al. (2007) Remote-sensing techniques for analysing landslide kinematics: A review. *Bulletin de la Société Geologique de France* 178: 89–100.

Dewitte O, Jasselette JC, Cornet Y, et al. (2008) Tracking landslide displacements by multi-temporal DTMs: A combined aerial stereophotogrammetric and LiDAR approach in western Belgium. *Engineering Geology* 99: 11–22.

Dikau R, Brunsden D, Schrott L, et al. (1996) *Landslide Recognition*. Chichester: Wiley.

d'Oleire-Oltmanns S, Marzolff I, Peter K, et al. (2012) Unmanned aerial vehicle (UAV) for monitoring soil erosion in Morocco. *Remote Sensing* 4: 3390–3416.

Doneus M, Verhoeven G, Fera M, et al. (2011) From deposit to point cloud – a study of low-cost computer vision approaches for the straightforward documentation of archaeological excavations. *Geoinformatics* 6: 81–88.

Dunford R, Michel K, Gagnage M, et al. (2009) Potential and constraints of Unmanned Aerial Vehicle technology for the characterization of Mediterranean riparian forest. *International Journal of Remote Sensing* 30: 4915–4935.

Fiorucci F, Cardinali M, Carla R, et al. (2011) Seasonal landslide mapping and estimation of landslide mobilization rates using aerial and satellite images. *Geomorphology* 129: 59–70.

Fonstad MA, Dietrich JT, Courville BC, et al. (2013) Topographic structure from motion: A new development in photogrammetric measurement. *Earth Surface Processes and Landforms* 38(4): 421–430.

Furukawa Y and Ponce J (2009) Accurate camera calibration from multi-view stereo and bundle adjustment. *International Journal of Computer Vision* 84: 257–268.

Furukawa Y and Ponce J (2010) Accurate, dense, and robust multi-view stereopsis. *IEEE Transactions on Pattern Analysis and Machine Intelligence* 32: 1362–1376.

Glenn NF, Streutker DR, Chadwick DJ, et al. (2006) Analysis of LiDAR-derived topographic information for characterizing and differentiating landslide morphology and activity. *Geomorphology* 73: 131–148.

Gorum T, Fan X, Van Westen CJ, et al. (2011) Distribution pattern of earthquake-induced landslides triggered by the 12 May 2008 Wenchuan earthquake. *Geomorphology* 133: 152–167.

Guzzetti F (2000) Landslide fatalities and the evaluation of landslide risk in Italy. *Engineering Geology* 58: 89–107.

Guzzetti F, Mondini AC, Cardinali M, et al. (2012) Landslide inventory maps: New tools for an old problem. *Earth-Science Reviews* 112: 42–66.

Harwin S and Lucieer A (2012) Assessing the accuracy of georeferenced point clouds produced via multi-view stereopsis from unmanned aerial vehicle (UAV) imagery *Remote Sensing* 4: 1573–1599.

Herman F, Anderson B and LePrince S (2011) Mountain glacier velocity variation during a retreat/advance cycle quantified using sub-pixel analysis of ASTER images. *Journal of Glaciology* 57: 197–207.

James MR and Robson S (2012) Straightforward reconstruction of 3d surfaces and topography with a camera: Accuracy and geoscience application. *Journal of Geophysical Research* 117: F03017.

Joyce KE, Belliss SE, Samsonov SV, et al. (2009) A review of the status of satellite remote sensing and image processing techniques for mapping natural hazards and disasters. *Progress in Physical Geography* 33: 83–207.

Kelcey J and Lucieer A (2012) Sensor correction of a 6-band multispectral imaging sensor for UAV remote sensing. *Remote Sensing* 4: 1462–1493.

Laliberte AS and Rango A (2009) Texture and scale in object-based analysis of subdecimeter resolution unmanned aerial vehicle (UAV) imagery. *IEEE Transactions on Geoscience and Remote Sensing* 47: 1–10.

Laliberte AS, Goforth MA, Steele CM, et al. (2011) Multispectral remote sensing from unmanned aircraft: Image processing workflows and applications for rangeland environments. *Remote Sensing* 3: 2529–2551.

Laliberte AS, Herrick JE, Rango A, et al. (2010) Acquisition, orthorectification, and object-based classification of Unmanned Aerial Vehicle (UAV) imagery for rangeland monitoring. *Photogrammetric Engineering and Remote Sensing* 76: 661–672.

Leprince S, Barbot S, Ayoub F, et al. (2007) Automatic and precise orthorectification, co-registration, and subpixel correlation of satellite images, application to

ground deformation measurements. *IEEE Transactions on Geoscience and Remote Sensing* 46: 1529–1558.

Leprince S, Berthier E, Ayoub F, et al. (2008) Monitoring earth surface dynamics with optical imagery. *EOS, Transactions American Geophysical Union* 89: 1–2.

Lowe D (2004) Distinctive image features from scale-invariant key points. *International Journal of Computer Vision* 60: 91–110.

Lucieer A, Turner D, King DH, et al. (2014) Using an Unmanned Aerial Vehicle (UAV) to capture micro-topography of Antarctic moss beds. *International Journal of Applied Earth Observation and Geoinformation*. 27(Part A): 53–62.

McIntosh PD, Price DM, Eberhard R, et al. (2009) Late Quaternary erosion events in lowland and mid-altitude Tasmania in relation to climate change and first human arrival. *Quaternary Science Reviews* 28: 850–872.

McKean J and Roering J (2004) Objective landslide detection and surface morphology mapping using high-resolution airborne laser altimetry. *Geomorphology* 57: 331–351.

Metternicht G, Hurni L and Gogu R (2005) Remote sensing of landslides: An analysis of the potential contribution to geo-spatial systems for hazard assessment in mountainous environments. *Remote Sensing of Environment* 98: 284–303.

Nadim F, Kjekstad O, Peduzzi P, et al. (2006) Global landslide and avalanche hotspots. *Landslides* 3: 159–173.

Neitzel F and Klonowski J (2011) Mobile 3D mapping with a low-cost UAV system. International Conference on Unmanned Aerial Vehicle in Geomatics (UAV-g), 14–16 September, Zurich. *International Archives of the Photogrammetry, Remote Sensing and Spatial Information Sciences* XXXVIII-1/C22: 39–44.

Niethammer U, James MR, Rothmund S, et al. (2012) UAV-based remote sensing of the Super-Sauze landslide: Evaluation and results. *Engineering Geology* 128: 2–11.

Niethammer U, Rothmund S, James MR, et al. (2010) UAV-based remote sensing of landslides. ISPRS Commission V Mid-Term Symposium 'Close Range Image Measurement Techniques', '21–24 June, 'Newcastle upon Tyne. *International Archives of the Photogrammetry, Remote Sensing and Spatial Information Sciences* XXXVIII, Part 5: 496–501.

Razak KA, Straatsma MW, van Westen CJ, et al. (2011) Airborne laser scanning of forested landslides characterization: Terrain model quality and visualization. *Geomorphology* 126: 186–200.

Scherler D, Leprince S and Strecker MR (2008) Glacier-surface velocities in alpine terrain from optical satellite imagery: Accuracy improvement and quality assessment. *Remote Sensing of Environment* 112: 3806–3819.

Schuster RL and Fleming WF (1986) Economic losses and fatalities due to landslides. *Bulletin of the Association of Engineering Geologists* 23: 11–28.

Snavely N, Seitz SM and Szeliski R (2008) Modeling the world from internet photo collections. *International Journal of Computer Vision* 80: 189–210.

Swiss Re (2011a) Flood risk on the rise in Brazil. Available at: http://www.swissre.com/rethinking/climate_and_natural_disaster_risk/Flood_risk_on_the_rise_in_Brazil.html.

Swiss Re (2011b) Natural catastrophes and man-made disasters in 2010. Sigma 1/2011. Available at: http:// media.swissre.com/documents/sigma1_2011_en.pdf.

Travelletti J, Delacourt C, Allemand P, et al. (2012) Correlation of multi-temporal ground-based optical images for landslide monitoring: Application, potential and limitations. *ISPRS Journal of Photogrammetry and Remote Sensing* 70: 39–55.

Triggs B, McLauchlan P, Hartley R, et al. (2000) Bundle adjustment: A modern synthesis. In: Triggs B, Zisserman A and Szeliski R (eds) *Vision Algorithms: Theory and Practice*. Berlin: Springer, 298–372.

Turner D, Lucieer A and Watson C (2012) An automated technique for generating georectified mosaics from ultra-high resolution Unmanned Aerial Vehicle (UAV) imagery, based on Structure from Motion (SfM) point clouds. *Remote Sensing* 4: 1392–1410.

van Westen CJ, Castellanos E and Kuriakose SL (2008) Spatial data for landslide susceptibility, hazard, and vulnerability assessment: An overview. *Engineering Geology* 102: 112–131.

Varnes DJ and International Association of Engineering Geology (IAEG) (1984) *Landslide Hazard Zonation: A Review of Principles and Practice*. Paris: UNESCO.

Ventura G, Vilardo G, Terranova C, et al. (2011) Tracking and evolution of complex active landslides by multi-temporal airborne LiDAR data: The Montaguto landslide (southern Italy). *Remote Sensing of Environment* 115: 3237–3248.

Verhoeven G (2011) Taking computer vision aloft – archaeological three-dimensional reconstructions from aerial photographs with photoscan. *Archaeological Prospection* 18: 67–73.

Westoby M, Brasington J, Glasser N, et al. (2012) 'structure-from-motion' photogrammetry: A low-cost, effective tool for geoscience applications. *Geomorphology* 179: 300–314.

Zarco-Tejada PJ, González-Dugo V and Berni JAJ (2011) Fluorescence, temperature and narrow-band indices acquired from a UAV platform for water stress detection using a micro-hyperspectral imager and a thermal camera. *Remote Sensing of Environment* 117: 322–337.

Zillman J (1999) The physical impact of disaster. In: Ingleton J (ed.) *Natural Disaster Management*. Leicester: Tudor Rose Holdings Ltd.